M&C 2017 - International Conference on Mathematics & Computational Methods Applied to Nuclear Science & Engineering, Jeju, Korea, April 16-20, 2017, on USB (2017)

Large Eddy Simulation of Turbulent Flows Using the CFD Code GASFLOW-MPI

Han Zhang, Jianjun Xiao, Thomas Jordan

Institute of Nuclear and Energy Technologies Karlsruhe Institute of Technology P.O. Box 3640, 76021 Karlsruhe, Germany
han.zhang@kit.edu, jianjun.xiao@kit.edu, thomas.jordan@kit.edu

Abstract - *GASFLOW-MPI is a scalable CFD software solution used to predict fluid dynamics, conjugate heat and mass transfer, chemical kinetics, aerosol transportation and other related phenomena. The generalized 3-D transient, compressible Navier-Stokes equations for multispecies are solved. It has been widely used to analyze safety problems in nuclear engineering. Turbulence models based on the Reynolds-Averaged Navier-Stokes (RANS) equations are implemented in the serial version of the 3-D CFD code GASFLOW. The computing power of the advanced parallel version of GASFLOW-MPI code has been greatly improved by using the message passing interface (MPI) and domain decomposition. In order to capture more details of turbulence and flow features in applications of scientific research and engineering problems, the large eddy simulation (LES) turbulent model is implemented in the advanced CFD parallel version GASFLOW-MPI. The standard Smagorinsky subgrid scale (SGS) model is utilized in the LES turbulence model. And the turbulent inflow boundary based on white noise is developed for LES to consider the turbulent intensity at the inlet. The parallelization technique based on PETSc library is described and the speed up ratio is analyzed. The preliminary validation of LES is carried out for a jet flow at high $Re=10^5$ and a backward-facing step flow at medium Re = 5100. The numerical results have been compared with the experimental data in literatures. Both time-averaged velocity profile and turbulent intensity are analyzed and agree well with the experimental data. Furthermore, the frequency spectrum is presented and a $-5/3$ energy decay is observed for a wide range of frequencies, satisfying the turbulent energy spectrum theory. Additional SGS models will be developed in GASFLOW-MPI while concentrating on the effects of chemical reactions and turbulent-shock interactions in subsonic and supersonic flows.*

Keywords: *GASFLOW-MPI, Large eddy simulation, Validation*

I. INTRODUCTION

The hydrogen will be generated during the severe accidents in nuclear power plants (NPPs) (Breitung, 1999) and may threaten the integrity of the containment, such as Fukushima accident in 2011. In the past decades, the CFD code GASFLOW [1,2] has been developed, validated and applied to simulate the complicated physical phenomena in reactor containments. The 3-D compressible multispecies Navier-Stokes equations are solved in GASFLOW. Different from most commercial CFD software, where one pressure-based algorithm is employed only for incompressible flow and another explicit density-based algorithm is utilized only for compressible flow, in GASFLOW a unified powerful "all-speed" flow algorithm "ICE'd ALE" is employed to solve a wide range of flows from incompressible limited flow to supersonic flow. Furthermore, GASFLOW has been widely used to analyze the hydrogen distribution and risk mitigation for different types of nuclear plants, such as the EPR [3], the International Thermonuclear Experimental Reactor (ITER) [4], the German Konvoi-Type PWR [5], the VVER [6], and the APR1400 [7]. Recently, the advanced parallel version of GASFLOW-MPI code had been developed and validated by the well-known test cases [8] and blind tests [9].

In order to mitigate hydrogen explosion risks in NPPs effectively, accurate predictions of the burnable hydrogen clouds distribution are crucial. It is well known that turbulence modeling is one of the key issues for a successful simulation of gas mixing and transport. However, only Reynolds-Averaged Navier-Stokes (RANS) based turbulent models are employed due to the limited computing capability in the serial version of GASFLOW. The computing power of the advanced parallel version of GASFLOW-MPI code has been greatly improved by using the message passing interface (MPI) and domain decomposition. In order to capture more details of turbulence and flow features in applications of scientific research and engineering problems, the large eddy simulation (LES) turbulent model has been developed in GASFLOW-MPI. The standard Smagorinsky subgrid scale (SGS) model is utilized in the LES turbulence model. And the turbulent inflow boundary based on white noise is developed to consider the turbulent intensity at the inlet. In this manuscript, a simulation of jet flow and backward-facing step flow have been performed by LES using GASFLOW-MPI.

This paper is organized as follows. The physical model in GASFLOW-MPI is presented in section II. The conservation equation, LES turbulent model and numerical methods are discussed here. The parallelization strategy of

GASFLOW and parallel computing capability are discussed in section III. The numerical results are presented and discussed in section IV. The conclusions are presented in section V.

II. PHYSICAL MODELS IN GASFLOW-MPI

1. Conservation Equation

GASFLOW-MPI is a scalable CFD software solution used to predict fluid dynamics, conjugate heat and mass transfer, chemical kinetics, aerosol transportation and other related phenomena. Since that only single phase, single component flows are simulated in this paper, the governing equation could be simplified as following for convenience. Here single component flow is considered, but heat/mass transfer, phase change and chemical reactions are not considered.

Volume equation

$$\frac{\partial V}{\partial t} = V\nabla\cdot\left(\mathbf{b}-\mathbf{u}\right) \tag{1}$$

where **b** is the control volume velocity surface vector incorporated in the simplified ALE methodology used in the GASFLOW code, **u** is the fluid velocity vector, and V is the discretized fluid control volume. When **b**=0 the equations are Eulerian, and when **b**=**u** the equations are Lagrangian.

Mass equation

$$\frac{\partial \rho}{\partial t} = \nabla\cdot\left[\rho\left(\mathbf{b}-\mathbf{u}\right)\right] \tag{2}$$

where ρ is the fluid density.

Momentum equations

$$\frac{\partial\left(\rho\mathbf{u}\right)}{\partial t} = \nabla\cdot\left[\rho\mathbf{u}\left(\mathbf{b}-\mathbf{u}\right)\right]-\nabla p+\nabla\cdot\boldsymbol{\sigma}+\rho\mathbf{g}-\nabla\cdot\tilde{\boldsymbol{\sigma}} \tag{3}$$

where p is the pressure, $\boldsymbol{\sigma}$ is the viscous stress tensor, **g** is the gravitational vector, and $\tilde{\boldsymbol{\sigma}}$ is the SGS Reynolds stresses term.

Internal energy equation

$$\frac{\partial\left(\rho I\right)}{\partial t} = \nabla\cdot\left[\rho I\left(\mathbf{b}-\mathbf{u}\right)\right]-p\nabla\cdot\mathbf{u}-\nabla\cdot\mathbf{q}-\nabla\cdot\tilde{\mathbf{q}} \tag{4}$$

where I is the fluid internal energy, **q** is the energy flux vector and $\tilde{\mathbf{q}}$ is the SGS heat flux term.

General thermodynamic equation of state

$$p = Z\left(\rho,T\right)\rho\frac{R}{M}T \tag{5}$$

where T is the absolute fluid temperature, R is the universal gas constant, M is the fluid molecular weight, and Z is the fluid compressibility factor.

General caloric equation of state

The gas specific internal energy I is a function which depends on gas density and absolute temperature.

$$I = I\left(\rho,T\right) \tag{6}$$

2. LES Turbulent Model

The SGS Reynolds stresses $\tilde{\boldsymbol{\sigma}}$ in momentum equation, resulting from filtering operations, are unknown, and therefore require modeling. Boussinesq hypothesis is employed to model the SGS turbulent stresses as follows.

$$\tilde{\sigma}_{ij} = -\mu_t\left(2S_{ij}-\frac{2}{3}S_{kk}\delta_{ij}\right) \tag{7}$$

where μ_t is the SGS turbulent viscosity and the rate-of-strain tensor S_{ij} is expressed as $S_{ij}=\left(\partial u_i/\partial x_j+\partial u_j/\partial x_i\right)/2$.

The Smagorinsky model is utilized to calculate the SGS turbulent viscosity, as shown in Eq. (8):

$$\mu_t = \rho L_s^2\left|S\right| \tag{8}$$

$$L_s = C_s\Delta \tag{9}$$

$$\Delta = V^{1/3} = \left(\Delta x\Delta y\Delta z\right)^{1/3} \tag{10}$$

$$\left|S\right| = \sqrt{2S_{ij}S_{ij}} \tag{11}$$

where L_s is the mixing length for subgrid scales and $\left|S\right|$ is an inner product of strain rate tensor, C_s is the Smagorinsky constant and Δ is the filter width. In theory, the Smagorinsky constant C_s is computed either from turbulence statistical theories or from DNS data base. In application, the Smagorinsky constant is set to 0.1 in this paper which has been found to yield the best results for a wide range of flows [10]. The filter width Δ is computed according to the volume of the compu-tational cell using Eq. (10).

In implementation, the effects of the SGS Reynolds stress are considered by utilizing the effective viscous stress tensor $\sigma_{eff,ij}$ as shown in Eq. (12).

$$\begin{aligned}\sigma_{eff,ij} &= \sigma_{ij}-\tilde{\sigma}_{ij} = \mu_{eff}\left(2S_{ij}-\frac{2}{3}S_{kk}\delta_{ij}\right)\\ &= \left(\mu+\mu_t\right)\left(2S_{ij}-\frac{2}{3}S_{kk}\delta_{ij}\right)\end{aligned} \tag{12}$$

where μ_{eff} is the effective viscosity coefficient.

The SGS heat flux term $\tilde{\mathbf{q}}$ in the energy equation is another unclosed term, and also requires approximation within the SGS model. The subgrid heat flux term is modeled using the gradient hypothesis and calculated by employing a turbulent Prandtl number Pr_t as follows [11].

$$\tilde{q}_j = -\lambda_t \frac{\partial T}{\partial x_j} \tag{13}$$

$$\lambda_t = \frac{\rho \mu_t}{\mathrm{Pr}_t} \tag{14}$$

where λ_t is the turbulent conductivity coefficient and Pr_t is the turbulent Prandtl number equaling to 0.90.

In implementation, the effective heat flux is utilized to consider the turbulent effects as follows.

$$q_{eff,j} = q_j + \tilde{q}_j = -\lambda_{eff} \frac{\partial T}{\partial x_j} = -\left(\lambda + \lambda_t\right) \frac{\partial T}{\partial x_j} \tag{15}$$

where λ_{eff} is the effective conductivity coefficient.

3. Numerical Method

A. ICE'd ALE Algorithm

ICE'd ALE is applicable for flows at all speeds, meaning from supersonic down to the incompressible limit. It is time-split into three distinct phases:

Phase A: An explicit Lagrangian phase where the diffusion terms and source terms are solved.

$$\frac{V^A - V^n}{\Delta t} = \sum_f \left(\mathbf{u}\cdot\mathbf{A}\right)_f^n \Delta S_f \tag{16}$$

$$\frac{\left(\rho V\right)^A - \left(\rho V\right)^n}{\Delta t} = 0 \tag{17}$$

$$\frac{\left(\rho V\mathbf{u}\right)^A - \left(\rho V\mathbf{u}\right)^n}{\Delta t} = -\sum_f \left[p_f^n + \left(\boldsymbol{\sigma}_{\mathbf{eff}}\mathbf{A}\right)_f^n \right] \Delta S_f + \rho \mathbf{g} V^n \tag{18}$$

$$\frac{\left(\rho V I\right)^A - \left(\rho V I\right)^n}{\Delta t} = -p^n \sum_f \left(\mathbf{u}\cdot\mathbf{A}\right)_f^n \Delta S_f - \sum_f \left(\mathbf{q}_{\mathbf{eff}}\cdot\mathbf{A}\right)_f^n \Delta S_f \tag{19}$$

$$p^A = \rho^A \frac{R}{M} T^A \tag{20}$$

where $\mathbf{A}$ is the outward normal fractional area vector.

Phase B: An implicit Lagrangian phase where pressure waves are propagated without time-step restrictions.

$$\frac{V^B - V^A}{\Delta t} = V^n \nabla\cdot\left[\left(\mathbf{u}\cdot\mathbf{A}\right)^B - \left(\mathbf{u}\cdot\mathbf{A}\right)^n\right] \tag{21}$$

$$\frac{\left(\rho V\right)^B - \left(\rho V\right)^A}{\Delta t} = 0 \tag{22}$$

$$\frac{\left(\rho V\mathbf{u}\right)^B - \left(\rho V\mathbf{u}\right)^A}{\Delta t} = -V^n \left[\nabla\left(p^B - p^n\right)\right] \tag{23}$$

$$\frac{\left(\rho V I\right)^B - \left(\rho V I\right)^A}{\Delta t} = -V^n p^n \nabla\cdot\left[\left(\mathbf{u}\cdot\mathbf{A}\right)^B - \left(\mathbf{u}\cdot\mathbf{A}\right)^n\right] \tag{24}$$

$$p^B = \rho^B \frac{R}{M} T^B \tag{25}$$

Defining $\delta p = p^n - p^B$, the elliptic pressure equation can be derived as

$$\Delta t^2 \nabla\cdot\left[\frac{\mathbf{A}V^n \nabla \delta p}{\left(\rho V\right)^A \left(1 + \frac{\Delta t \mathbf{C}_d \left|\mathbf{u}^n\right|}{2\Delta x}\right)}\right] - \frac{V^A}{V^n\left(p^A + C\right)}\delta p = \frac{V^A\left(p^n - p^A\right)}{V^n\left(p^A + C\right)} + \Delta t \nabla\cdot\left[\left(\left(\mathbf{u}\cdot\mathbf{A}\right)^A - \left(\mathbf{u}\cdot\mathbf{A}\right)^n\right)\right] \tag{26}$$

where the coefficient, for an ideal gas, is

$$C = p^n \left(\frac{R}{M\cdot c_v\left(T\right)}\right)^A \tag{27}$$

Phase C: An explicit convection (rezone or remapping) phase.

$$V^{n+1} = V^n \tag{28}$$

$$\frac{\left(\rho V\right)^{n+1} - \left(\rho V\right)^B}{\Delta t} = -\sum_f \left(\rho \mathbf{A}\cdot\mathbf{u}\right)_f^B \Delta S_f \tag{29}$$

$$\frac{\left(\rho V\mathbf{u}\right)^{n+1} - \left(\rho V\mathbf{u}\right)^B}{\Delta t} = -\sum_f \left(\rho \mathbf{A}\cdot\mathbf{u}\cdot\mathbf{u}\right)_f^B \Delta S_f \tag{30}$$

$$\frac{\left(\rho V I\right)^{n+1} - \left(\rho V I\right)^B}{\Delta t} = -\sum_f \left(\rho \mathbf{A}\cdot\mathbf{u} I\right)_f^B \Delta S_f \tag{31}$$

$$p^{n+1} = \rho^{n+1} \frac{R}{M} T^{n+1} \tag{32}$$

B. Van Leer Algorithm and Flux Limiter

A second order accuracy scheme, the well-known van Leer MUSCL scheme, is adopted for convection term in this paper [1]. To illustrate the van Leer algorithm, we first expand the right-hand side of the species mass, momenta, and energy in Equations (29) through (31) over the finite-volume control surfaces as

$$\sum_f \left(\phi A u\right)_f^B \Delta S_f = \begin{cases} \left\langle \phi A u\right\rangle_E^B \delta y \delta z - \left\langle \phi A u\right\rangle_W^B \delta y \delta z + \\ \left\langle \phi A v\right\rangle_N^B \delta x \delta z - \left\langle \phi A v\right\rangle_S^B \delta x \delta z + \\ \left\langle \phi A w\right\rangle_T^B \delta x \delta y - \left\langle \phi A w\right\rangle_B^B \delta x \delta y \end{cases} \tag{33}$$

where ϕ is, respectively, ρ , $\rho\mathbf{u}$, and ρI . We remind the reader that A is the fractional area open for flow on that particular surface. The East (E) surface of computation

volume (I, J, K) corresponding with the mass and energy equations coincides with the indexing notation of i+1/2, where the special notation $\langle\bullet\rangle$ is defined:

$$\langle \phi A u\rangle^B_{i+\frac{1}{2}} = \begin{cases} A_{i+\frac{1}{2}} u^B_{i+\frac{1}{2}} \left\{ \phi^B_i + \frac{1}{2}\left[\delta x_i - u^B_{i+\frac{1}{2}} \delta t \right] S_i \right\}; u^B_{i+\frac{1}{2}} \ge 0 \\ A_{i+\frac{1}{2}} u^B_{i+\frac{1}{2}} \left\{ \phi^B_{i+1} + \frac{1}{2}\left[\delta x_{i+1} + u^B_{i+\frac{1}{2}} \delta t \right] S_{i+1} \right\}; u^B_{i+\frac{1}{2}} \le 0 \end{cases}$$

$$\text{where} \begin{cases} S_i = \dfrac{\phi^B_{i+1} - \phi^B_{i-1}}{\delta x_{i+\frac{1}{2}} + \delta x_{i-\frac{1}{2}}}; u^B_{i+\frac{1}{2}} \ge 0 \\ S_{i+1} = \dfrac{\phi^B_{i+2} - \phi^B_i}{\delta x_{i+\frac{3}{2}} + \delta x_{i+\frac{1}{2}}}; u^B_{i+\frac{1}{2}} \le 0 \end{cases} \quad (34)$$

By limiting the value of the slope in various situations, we can impose the monotonicity condition. Basically, the monotonicity condition states that when the initial conditions for a particular variable are monotone, the time-advanced values are also monotone. In other words, if ϕ^B_i lies between ϕ^B_{i-1} and ϕ^B_{i+1}, then ϕ^{n+1}_i must lie between ϕ^{n+1}_{i-1} and ϕ^{n+1}_{i+1}.

$$(S_i)_{mon} = \begin{cases} sign\left(\phi^B_{i+1} - \phi^B_{i-1}\right) \cdot \min\left(Slop^i_{i-1}, Slop^{i+1}_{i-1}, Slop^{i+1}_i\right); \\ if: sign\left(\phi^B_i - \phi^B_{i-1}\right) = sign\left(\phi^B_{i+1} - \phi^B_{i-1}\right) \\ = sign\left(\phi^B_{i+1} - \phi^B_i\right) \\ 0; \ otherwise \end{cases} \quad (35)$$

$$(S_{i+1})_{mon} = \begin{cases} sign\left(\phi^B_{i+2} - \phi^B_i\right) \cdot \min\left(Slop^{i+1}_i, Slop^{i+2}_i, Slop^{i+2}_{i+1}\right); \\ if: sign\left(\phi^B_{i+1} - \phi^B_i\right) = \\ sign\left(\phi^B_{i+2} - \phi^B_i\right) = sign\left(\phi^B_{i+2} - \phi^B_{i+1}\right) \\ 0; \ otherwise \end{cases} \quad (36)$$

$$Slop^i_{i-1} = \left(\frac{\phi^B_i - \phi^B_{i-1}}{\delta x_{i-\frac{1}{2}}} \right), Slop^{i+1}_{i-1} = \left(\frac{\phi^B_{i+1} - \phi^B_{i-1}}{\delta x_{i+\frac{1}{2}} + \delta x_{i-\frac{1}{2}}} \right),$$

$$Slop^{i+1}_i = \left(\frac{\phi^B_{i+1} - \phi^B_i}{\delta x_{i+\frac{1}{2}}} \right), \ Slop^{i+2}_i = \left(\frac{\phi^B_{i+2} - \phi^B_i}{\delta x_{i+\frac{3}{2}} + \delta x_{i+\frac{1}{2}}} \right), \quad (37)$$

$$Slop^{i+2}_{i+1} = \left(\frac{\phi^B_{i+2} - \phi^B_{i+1}}{\delta x_{i+\frac{3}{2}}} \right)$$

III. PARALLELIZATION OF GASFLOW

Serial version GASFLOW is a well-developed practical simulator to analyze the hydrogen safety of various nuclear reactor types [3-7] in the past decades, as mentioned in Section I. Furthermore, GASFLOW has been widely utilized by the nuclear engineers in several European and Asian countries. However, GASFLOW was originally designed as a sequential CFD code. Several months should be taken for a typical LOCA scenario (10,000 seconds) of PWR containment with around 300,000 cells. Obviously, the original serial computational capability could not meet the requirements of large-scale nuclear engineering problems. Therefore, the parallel version GASFLOW: GASFLOW-MPI was started to develop based on the paradigms of Message Passing Interface (MPI) and domain decomposition in 2013. In GASFLOW-MPI, the data structure (including vector and matrix), parallel linear solvers and preconditioners are implemented based on the library Portable Extensible Toolkit for Scientific Computing (PETSc) [12]. Recently, the new developed code GASFLOW-MPI have been validated by the well-known test cases [8] and blind tests [9]. Parallelzation of GASFLOW could significantly reduce the computational time of large scale industrial simulations, as shown in section 3.2. GASFLOW-MPI could also make great contribution to the large scale industry simulations. It enables the creation of large scale and high-fidelity models which provide more accurate and detailed predictions, such as the new developed LES turbulent model in this paper.

1. Parallelization of GASFLOW Based on PETSc Library

PETSc is one of the most widely used software library for high-performance computational science, which is developed at Argonne National Laboratory. Many scientific applications have been built based on PETSc, such as the multi-physical coupling platform MOOSE in Idaho National Laboratory [13], the finite element package libmesh [14] and so on. PETSc can be used for application codes written in Fortran, C, C++, Python and Matlab. And the parallel communication in PETSc is achieved based on MPI. It can provide numerical infrastructure for application codes, from the basic data structures to the advanced preconditioned linear and nonlinear solvers, as shown in Fig.1. The main advantage of PETSc is that the application programmers could be freed from writing the sophisticated message-passing codes and only concentrate on the physics modeling development, because the detailed message passing required during the coordination of the computations is handled inside the PETSc library.

GASFLOW-SEQ is written in Fortran 90 with more than 120,000 lines and 634 subroutines in version 3.5. A semi-implicit pressure-based methodology [1] is employed in GASFLOW, and an elliptic pressure equation is required to solve at each time step. Therefore, a linear solver should be utilized to solve the symmetrically sparse linear equation system derived from the discretizated elliptic pressure equa-

tion. As the original linear solver in GASFLOW-SEQ is not suitable for scalable parallelization [8], all the programs relevant to the original linear solver should be rewritten. As a result, the parallelization of GASFLOW focus on two main tasks. The first one is the parallelization of all the data structures in the original GASFLOW-SEQ. The second one is that an efficient scalable linear solver is necessary to solve the large scale symmetrically sparse linear equation system.

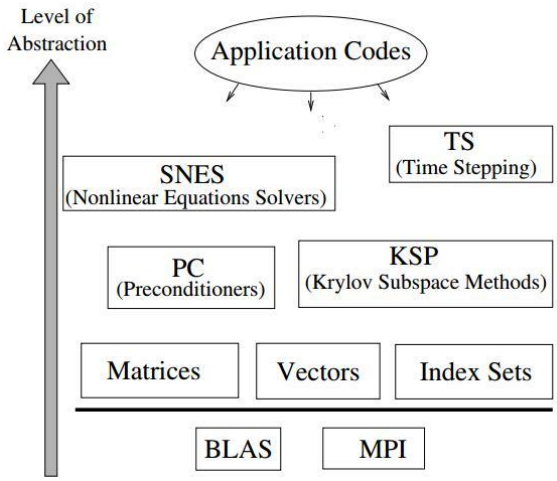

Fig. 1. Organization of the PETSc Library [12]

PETSc provides a data management object, DMDA, which contains the parallel regular arrays layout and manages the parallel communication based on the domain decomposition technique. Considering the structured grid is used in GASFLOW code, the data object DMDA is employed for the parallelization of arrays in the original GASFLOW-SEQ. It should be noted that a staggered grid is adopted in the GASFLOW code, while the PETSc data management object DMDA is designed for collocated grid arrangement. As a result, special treatment should be taken to utilize the data structure object in PETSc.

The efficient scalable linear solver is another key issue for the parallelization of GASFLOW. A large scale symmetrical sparse linear equation system should be solved per time step. Several advanced Krylov subspace methods and scalable preconditioning methods are provided in PETSc to solve this large scale elliptic pressure equation. We have tested different Krylov subspace methods like conjugate gradient (CG), conjugate residual (CR), minimal residual method (MINRES) and SYMMLQ, and the preconditioners like point Jacobi, point Gauss-Seidel, block Jacobi and additive Schwarz method (ASM). The computational performance of CG solver preconditioned by block Jacobi method is the most efficient combinations in our test cases. Therefore, the CG together with block Jacobi is the default solver for the elliptic pressure equation in the current GASFLOW-MPI. Future code development will focus on more efficient preconditioners in scientific libraries, such as the algebraic multigrid (AMG) preconditioner in Hypre, which can further improve the performance of GASFLOW-MPI code.

2. Parallel Scalability of GASFLOW-MPI

The parallel scalability test is performed in this section. It is well known that the parallel scalability test of linear solver for the elliptic pressure equation is the key point. In order to overweigh the computational cost of the linear solver, a hypothetical 3-D H_2 bubble in mixture of air, steam and liquid droplets is performed. In this case, the pressure field changes drastically per time step. Therefore, a considerable number of iterations are required to achieve convergence. Furthermore, in order to overweigh the other communication costs, most of the features in GASFLOW-MPI are switched on, such as the convection heat transfer term, radiation heat transfer term and the diffusion terms in the mass/momentum/energy equations. In this case, the total number of computational nodes is 8,000,000. And the converence criterion of the linear solver is 1.0e-8.

The parallel scalability performance is implemented on our server. The server has Intel Xeon Processor E5-2667 v2 CPU with 3.3 GHz frequency. There are totally 8 nodes with 16 cores on each of them. Each node has 32 GB DDR3-1866 MHz memory [8]. In order to eliminate the effect of the limited memory bandwidth per core, the number of processes increases from 16 to 128 at intervals of 16. Fig. 2 demonstrates the speed-up relative to one node (16 processes). In our 3-D problem with 8,000,000 cells, a linear scaling is achieved based on the multiples of 16 processes. The computational performance of 128 processes is about 8 times higher than that of 16 processes. Furthermore, an extra speed-up is also observed in Fig. 2. One possible reason could be that with more processes the working set can fit better into the caches and reduce the memory access time. Another possible reason is that more processes make decomposed domains more uniform and the computational load is more balanced. The further discussion about the parallel scalability of the GASFLOW-MPI could be found in Refs [8].

IV. EXPERIMENTAL RESULTS

In this section, we present the main results of our GASFLOW-MPI simulations using LES turbulent model. The first case is a 3-D round jet flow which is a fundamental physical phenomenon in hydrogen safety analysis. The second case is the backward-facing step flow which is a standard benchmark to validate the turbulence model.

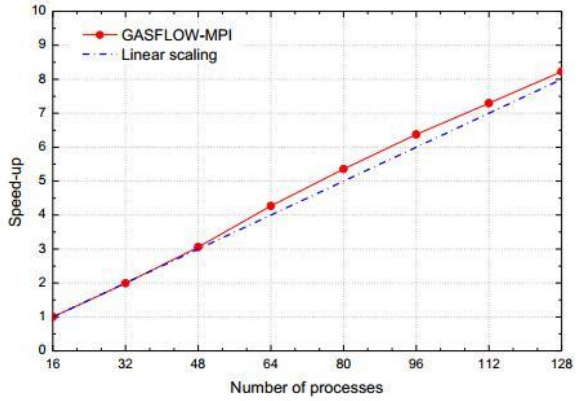

Fig. 2. Speed-up relative to one node (16 processes)

1. Jet Flow Case

In the practical hydrogen safety analysis in nuclear engineering, due to the complexity of the structures and installations around the break, there is a wide spectrum of gas flow in the containment, such as under-expanded jets, impinging jets and plumes. However, a fundamental physical phenomenon is the jet flow. Furthermore, extensive experimental research has been conducted on this flow, allowing comparisons. In this section, a high Reynolds ($Re=10^5$) jet flow is implemented to validate the new developed LES turbulent model in GASFLOW-MPI.

A. Problem Description

The computational domain and the boundary condition used for this simulation are shown in Fig. 3. The cylindrical coordinate is employed. The longitudinal length L_x downstream is $23.75D$, and radial length L_r is $5.5D$ where D is the diameter of the inlet jet. The velocity boundary is used as the inlet boundary. The profile of the inlet velocity is an important issue for a successful simulation of jet flow. The inlet velocity is 56.2m/s. In this case, the velocity profile is calculated by Eq.(38). Zero-gradient boundary, also called continuous boundary condition, is posed at the other boundaries, as shown in Fig. 3.

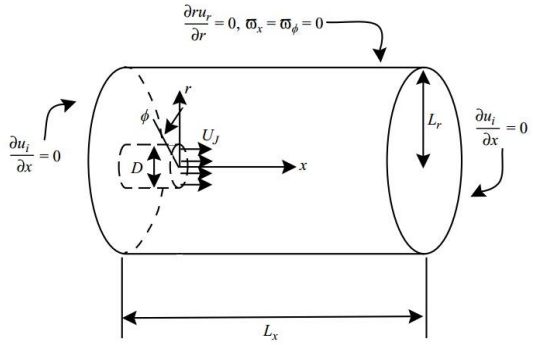

Fig. 3. Jet flow configuration

$$u(r)=\frac{U_{inlet}}{2}\left\{1+\tanh\left[\frac{D-2r}{4\theta_m}\right]\right\} \tag{38}$$

where θ_m is the momentum thickness of the shear layer at the nozzle exit, and $D/\theta_m=40$ in this case.

The uniform grid spacing is selected for the stream-wise and azimuthal directions and a non-uniform grid spacing is used for radial direction which is refined at the inlet boundary. The number of grid points is equal to 192 × 128 × 64 points in the axial, radial, and azimuthal direction respectively. The distribution of the mesh size in the radial direction is shown in Fig. 4. The minimum mesh size is about $0.015D$ near the free shear layer and the maximum mesh size is about $0.045D$.

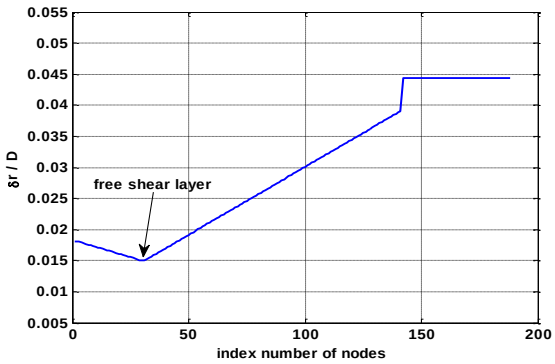

Fig. 4. Radial mesh size distribution

The time step in the current simulation is self-adjusted to limit the CFL number below 0.25. The maximum CFL is set to 0.25 in order to capture the fluctuation information even though larger CFL numbers can be used.

B. Numerical Results Analysis

The results obtained from the LES of a spatially developing circular jet at a Reynolds number of 10^5 are discussed here. The standard Smagorinsky model is used for the resolution of the SGS model within the filtered NS equations. With the help of instantaneous and time-averaged flow data, the spatial transition from the laminar state to the turbulent is analyzed. The time-averaged radial velocity profile is examined for self-similarity. The turbulence intensity $\overline{u'^2}$, $\overline{v'^2}$, and $\overline{w'^2}$ are presented and compared with the data available in the literature. It should be noted that the averaged parameters are averaged in time and along the azimuth direction.

The Fig. 5 represents the instantaneous velocity distribution in *r-azimuth* plane. From the physical experience, the averaged velocity profile should be symmetrical in azimuth direction. However, due to the turbulent fluctuations, the instantaneous velocity distribution is no longer symmetrical in azimuth direction. This phenomenon can't be captured in the original RANS model. The Fig. 6 shows the velocity

distribution in *r-x* plane. Apparently, the flow could be divided into several regions according to the flow state. Firstly, the flow near the inlet is the steady axisymmetric laminar state which is called the potential core region. At the end of the potential core, interaction among flow structures leads to a transition from the laminar state to the turbulent state in the transition region, and then the turbulence is fully developed in the fully developed region. And complex eddy structure could be observed in the transition region and fully developed region. However, the information about eddy structure cannot be provided in the RANS model since the Reynolds-averaged Navier-Stokes is solved in the RANS model and all the eddy behavior is averaged.

In Fig. 7 we show the velocity profile in the centerline. The slopes of the decay line of the streamwise velocity are comparable for Reynolds numbers of 103000 [15], 32000 and 64000 [16] (experiments) with Re = 10^5 (LES), as shown in Fig. 7. In the potential core region, it is laminar state, and the size of streamwise velocity is almost kept as a constant. And then the flow field begins to transfer from laminar into turbulence when it is in the transition region. At the same time, the size of streamwise velocity starts to decay. In this case, the length of the potential core obtained from the simulation is about 5D which agrees with the experimental range of $4 < x/D < 5.5$ [15]. In general, the simulation result agrees quite well with the data sets over all regions.

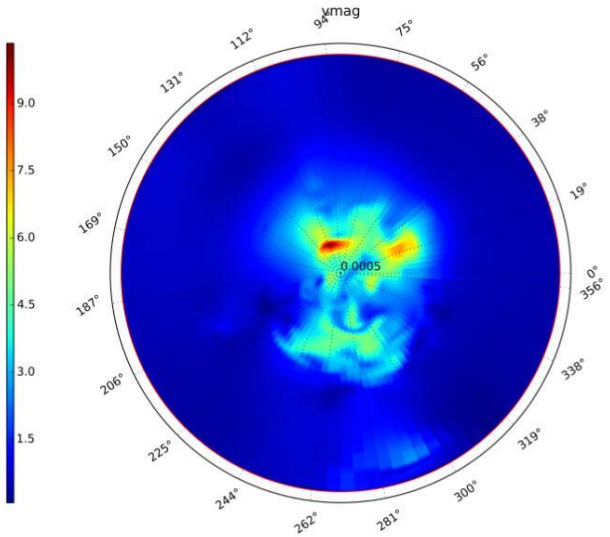

Fig. 5 Instantaneous velocity distribution in r-azimuth plane

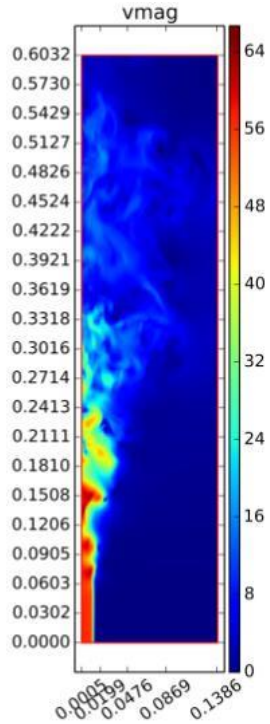

Fig. 6 Instantaneous velocity distribution in r-x plane

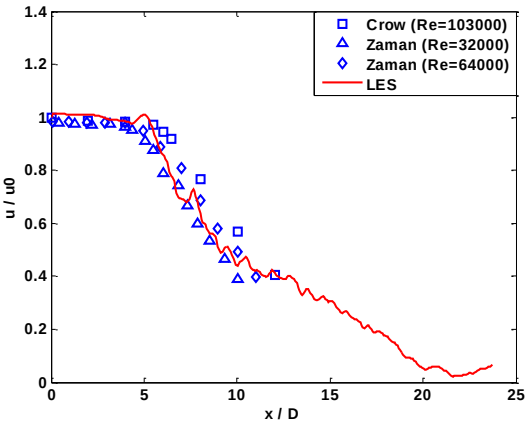

Fig. 7. Time-averaged streamwise velocity

The time-averaged velocity profiles in r direction are presented and compared the experimental data from Hussein et al [17]. The normalized time-averaged velocity profile $u(r)/U_0$ in the fully developed region could be expressed as a Gaussian function based on the nondimensional radial coordinate $\eta = r/(x-x_0)$. The profiles at several downstream locations $x/D = 17.0, 18.5, 20.0$ are compared with the experimental self-similar data available in the literature [17], as shown in Fig. 8. The results show that the simulated velocity profiles at different downstream locations reach the

self-similar state and agree quite well with the experiment data sets.

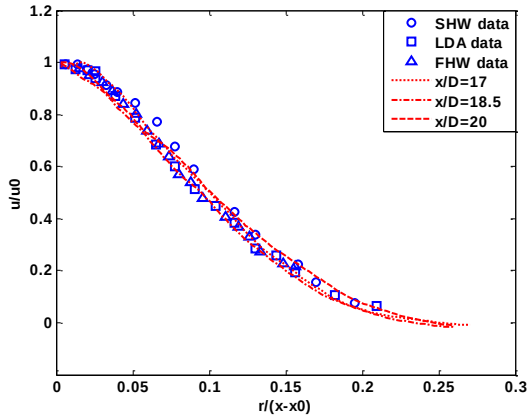

Fig. 8. Radial variation of the time-averaged streamwise velocity profiles

For a better understanding of the evolution of turbulent jet flow, longitudinal $\overline{u'^2}$, radial $\overline{v'^2}$ and azimuthal $\overline{w'^2}$ turbulent intensities computed with the current LES are presented in Fig. 9. All the turbulent intensities reach the maximum value at the center line, and then gradually decreases with the increase of the radius. The computational results are also compared with the experimental data [17], where the turbulent intensities are nondimensionalized using the square of the local centerline velocity U_0. The computational turbulence intensity predicts well with the experimental data. It should be noted that the turbulent information at large eddy scale could be resolved directly in LES model, however, all the turbulent information is modeled in the RANS turbulent model. As a result, the LES turbulent model could capture more detail turbulent information and the LES is more general than RANS.

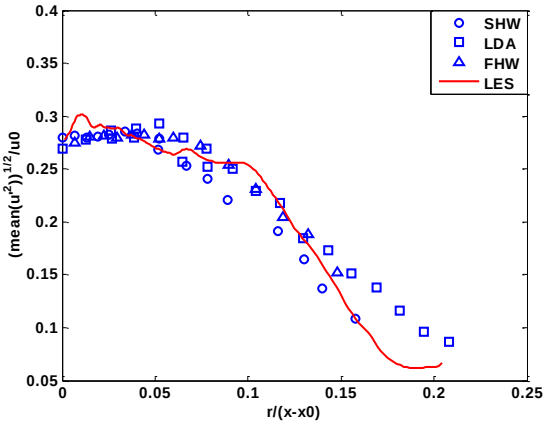

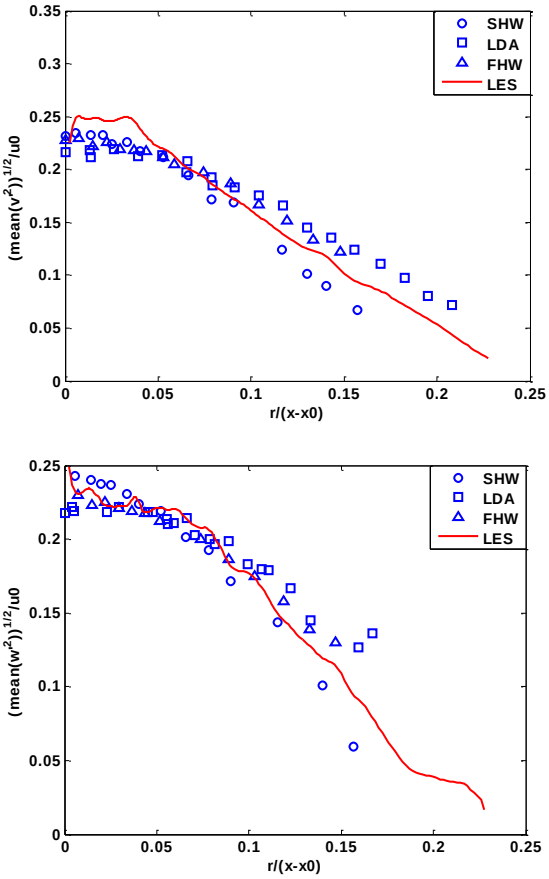

Fig. 9. Radial variation of the Reynolds stress components (top) longitudinal, (middle) radial, and (bottom) azimuthal

2. Backward-Facing Step Flow Case

The backward facing step is chosen for its apparent geometrical simplicity, but it involves relatively complex flow phenomena. This geometry is well suited to study the turbulence behavior under separation, recirculation and reattachment phenomena, which are highly important for many practical and engineering applications. Furthermore, extensive experimental research on this flow has been conducted, and a large bibliographic data base exists, allowing comparisons. In this paper, the backward facing step flow at Re=5100 is simulated by LES turbulent model in GASFLOW-MPI and the results are compared with the Jovic and Driver's experiment [18].

A. Problem Description

The computational domain used for this simulation is shown in Fig. 10. The longitudinal length L_x downstream of the step is $20h$, where h is the step height, and channel length L_i, ahead of the step is $10h$. The dimensions in the vertical L_y and spanwise L_z directions are $6h$ and $4h$ respectively. The uniform grid spacing is selected for the

streamwise and spanwise directions and a non-uniform grid spacing is used for vertical direction which is refined near the lower wall and at the step in the vertical direction. And a total number of 1.2 million computational cells are utilized in this simulation.

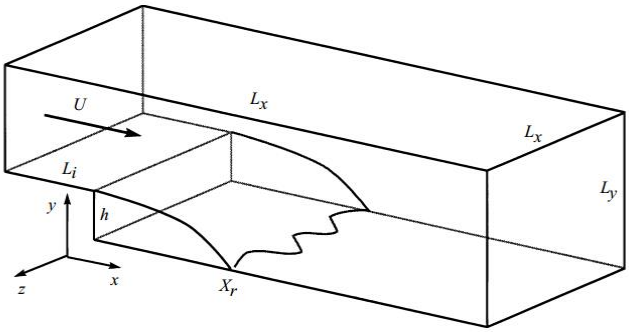

Fig. 10. Backward-facing step flow configuration

In this case, the turbulent velocity boundary is employed as the inlet boundary, as shown in Eq.(39). The u , v and w are velocity components in longitudinal, vertical and spanwise direction respectively. The mean turbulent profile $u^{mean}(y,z)$ by Spalart [19] at $\mathrm{Re}_\theta = 670$ is superimposed at inlet where θ is the momentum thickness. The boundary layer thickness at the inlet is $\delta_{99} = 1.2h$. The mean u out-side the boundary layer is 7.72m/s. The mean values for v and w are set equal to zero. The turbulent information is a key issue to successfully simulate this flow. In this paper, the turbulent fluctuation $u'(y,z)$ is modeled based on the white noise method, as shown in Eq.(40). A no-stress wall $v = 0, \partial u/\partial y = 0, \partial w/\partial y = 0$ is applied at the upper boundary and spanwise boundaries, while no-slip boundary conditions are used at all other horizontal walls. A continuous boundary is employed at the outflow boundary, which means the outflow is completely developed and the velocities gradients $\partial u_i / \partial x_i$ are set equal to zero.

$$u(y,z) = u^{mean}(y,z) + u'(y,z) \tag{39}$$

$$u'(y,z) = \sqrt{\frac{3}{2}k} \cdot \varepsilon \tag{40}$$

where k is the turbulent energy at the inlet and ε is the random number obeying standard normal distribution.

The uniform grid spacing is selected for the streamwise and spanwise directions and a non-uniform grid spacing is used for vertical direction. Specifically, a total of 384 computational cells are used in the *x*-direction and 32 cells in the *z*-direction. In the vertical direction, a non-uniform mesh distribution is used with fine grid spacing near the lower wall and at the step. Fig. 11 shows the mesh distribution for the wall-normal direction with refined grid at the wall in the inlet section ($y = h$) and at the lower wall ($y = 0$), downstream of the step. The total number of computational cells in the vertical direction is 96, of which 35 are placed within the step ($y < h$). The grid spacings in the three directions in wall units are $\Delta x_+ \approx 20$, $\Delta y_{min+} \approx 0.6$, $\Delta y_{max+} \approx 62$, and $\Delta z_+ \approx 30$, respectively, based on the inlet boundary layer shear velocity, $u_{\tau 0}$. The time step in the current simulation is self-adjusted to limit the CFL number below 0.25.

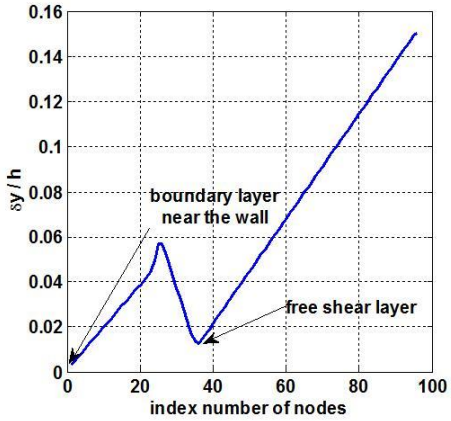

Fig. 11 Mesh distribution in the wall-normal direction

The viscous stress treatment near the wall is also an important issue to simulate the profile within the boundary layer accurately. In this paper, the grid spacing is fine enough to resolve the profile within the boundary layer. Therefore, a direct discretization of the viscous stress term is utilized, as shown in Eqs.(41-42), rather than a wall function.

$$\left(\sigma_{ij} \mathrm{A}_j\right)\Big|_{\mathrm{wall}} = \mu \left[\left(\frac{\partial u_i}{\partial x_j} + \frac{\partial u_j}{\partial x_i}\right)\right]_{\mathrm{wall}} \mathrm{A}_j = \tau_w \mathrm{A}_j ; \; i \neq j \tag{41}$$

$$\left.\frac{\partial v}{\partial x}\right|_{wall} = \frac{v}{\Delta x/2}, \quad \left.\frac{\partial w}{\partial x}\right|_{wall} = \frac{w}{\Delta x/2} \tag{42}$$

B. Numerical Results Analysis

LES simulation over a backward facing step is carried out and discussed in this section. Firstly, the characteristics of the unsteady flow are analyzed. And then, different flow parameters, reattachment length, mean longitudinal velocity profiles and turbulent intensity are computed and compared with experiment of Jovic et al. [18]. These parameters are averaged in time and along the spanwise direction. The mean longitudinal, vertical velocity profiles and turbulent intensity are non dimensionalized with the inflow free stream velocity U_0. Lastly, the frequency spectrum of velocity fluctuations is computed and compared with theory frequency spectrum.

The eddy behavior is resolved by the LES method, as shown in Fig.12. The oscillatory flow behavior is a phenomenon that is not observed in the RANS model, because all

the velocity fluctuations are also averaged in the RANS model, and only time-averaged results could be resolved. However, the reattachment location always varies over time in a certain region due to the velocity fluctuation, as shown in Fig.12. A similar phenomenon is observed and analyzed in previous investigations [18].

The mean reattachment location, Xr, is computed by the four methods as proposed by Le et al. [20]. All of these methods are equivalent: (a) the longitudinal distance where $\tau_w = 0$; (b) the location at which the mean dividing streamline ($\psi = 0$) touches the wall; (c) the location at which the mean longitudinal velocity $u = 0$ at the first grid point away from the wall; and (d) the mean reattachment point which is indicated by the location of 50% forward flow fraction using the p.d.f. method. The third method is employed in this paper. The computed reattachment length is Xr=6.9h which is consistent with the LES result Xr=6.8h of [21,22], the DNS result Xr=6.28h of Le et al. [20] and the experimental value (Xr=$(6\pm0.15)h$) [18].

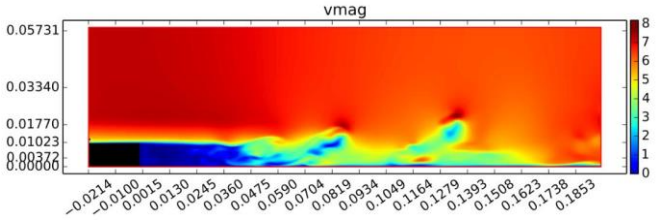

(a) Instantaneous velocity at 0.40s

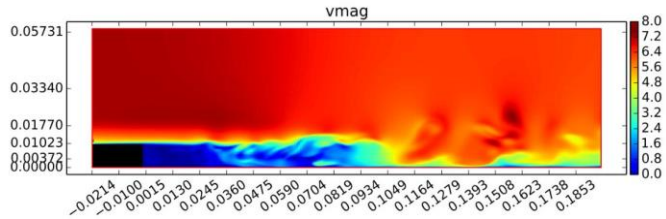

(b) Instantaneous velocity at 0.50s

Fig. 12. Velocity distribution

Westphal and Johnston [23] concluded that the averaged velocity is independent of the initial conditions, geometrical parameters and boundary conditions with respect to the normalized coordinate $X^* = (x - Xr)/Xr$. These results are further confirmed by Dubief and Delcayre [24], Aider and Danet [25] and Panjwani [26]. In this paper, the normalized coordinates X^* are utilized for comparison of our LES results with the experiment of Jovic et al. [18]. The comparisons are implemented between computed LES results and the experiments data by Jovic et al for the non-dimensional mean longitudinal velocity, as shown in Fig.13. Three locations are used to make the comparison: (a) where the recirculation ($X^* = -0.333$) is located: (b) where the reattachment ($X^* = 0.000$) is located; and (c) where the recovery region ($X^* = 0.666$) is located. The computed results agree well with the experimental data at all three different locations. Especially, the longitudinal velocity in the recirculation region where $y/h < 0.5$ is in good agreement with the experimental data.

The averaged longitudinal $\overline{u'^2}$, vertical turbulent $\overline{v'^2}$ intensities and the Reynolds shear stress component $\overline{u'v'}$ computed with the current LES are compared with the experimental data, as shown in Fig.14, where u' and v' are the velocity fluctuation in longitudinal and vertical direction, respectively. The comparison is made at the same three locations. The computational turbulence intensity predicts well with the experimental data.

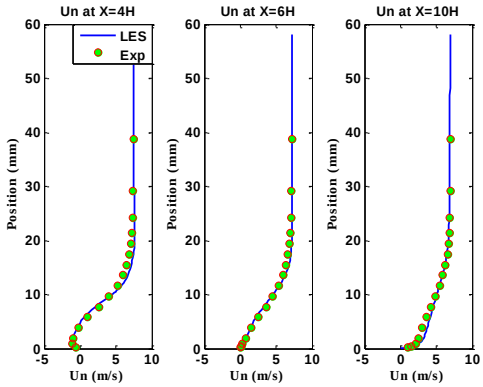

Fig. 13. Mean longitudinal velocity profiles at three different streamwise positions

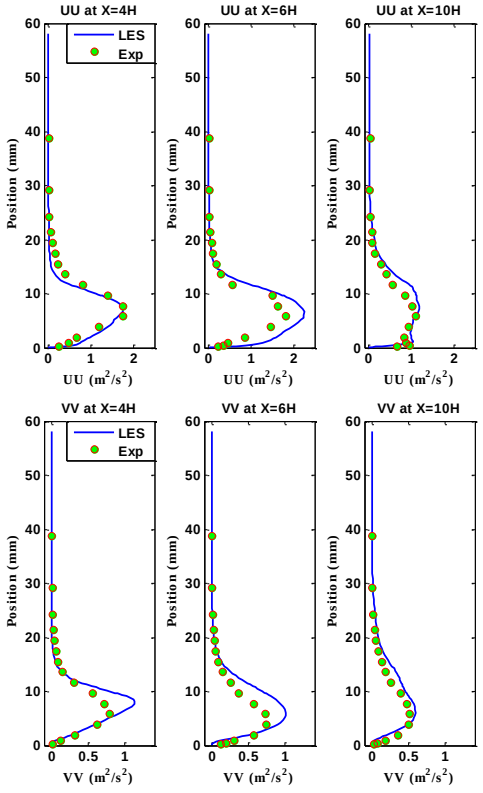

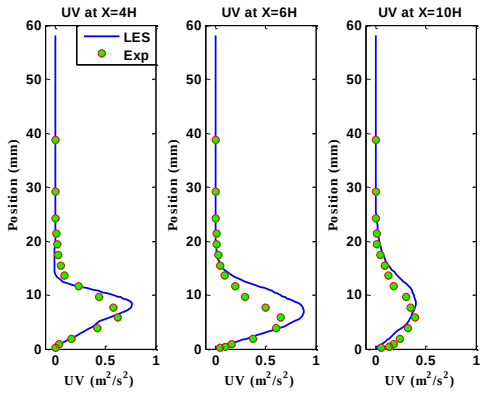

Fig. 14. Square roots of Reynolds stresses components: (top) $\overline{u'^2}$, (middle) $\overline{v'^2}$, and (bottom) $\overline{u'v'}$ at three different streamwise positions.

The sign of the longitudinal velocity fluctuations during the period between 0.3s and 1.0s is plotted in Fig.15(a). The distribution of the velocity fluctuations is random, which is not captured by the RANS model. The frequency spectrum is analyzed, as shown in Fig.15(b). In the corresponding energy spectrum, we observe a $-5/3$ energy decay for a wide range of frequencies (red line), followed by a steeper decay for $f > 10^3$, as characteristic for the energy cascade decay in turbulence. And it also indicates that most turbulent energy is contained in lower frequencies, satisfying the turbulent energy spectrum theory.

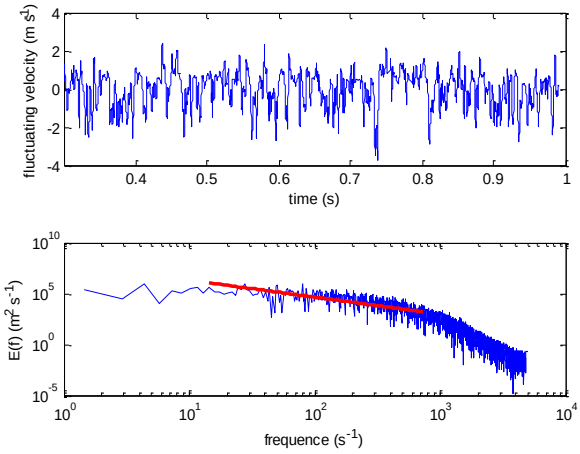

Fig. 15. Frequency spectrum of velocity fluctuations

V. CONCLUSIONS

A large eddy simulation (LES) turbulent model is implemented in the advanced CFD parallel version GASFLOW-MPI. The parallelization technique based on PETSc library is described and the speed up ratio is also analyzed. The standard Smagorinsky subgrid scale (SGS) model is utilized in the LES turbulence model. The turbulent inflow boundary based on the white noise is developed. The preliminary validation of LES is carried out for a jet flow at high Re=10^5 and a backward-facing step flow at medium Re = 5100.

For the jet flow case, both time-averaged quantity and turbulent quantity are analyzed. Eddy structure is observed in LES model which cannot be captured in RANS model. Time-averaged streamwise velocity in the centerline agrees well with the experimental data. And the time-averaged axial velocity profile is examined for self-similarity using the experimental data. The turbulence intensity $\overline{u'^2}$, $\overline{v'^2}$, and $\overline{w'^2}$ agree well with the data available in the literature.

For the backward-facing step flow, the mean quantities and turbulent quantities are represented and discussed. The turbulent inflow boundary condition is utilized in this paper. The reattachment length in the longitudinal direction is Xr=6.9h which is consistent with the other LES results, DNS result and experimental data. The mean velocity profile, turbulence intensity and the Reynolds stresses are aligned with the experimental data set. The frequency spectrum for the longitudinal velocity fluctuations u' is analyzed. A $-5/3$ energy decay is observed for a wide range of frequencies, and it also indicates that most turbulent energy is contained in low frequencies.

More SGS models will be developed in GASFLOW-MPI: concentrating on the effects of chemical reactions, and turbulence-shock interaction in subsonic and supersonic flows.

REFERENCES

1. J. Xiao, J.R. Travis, T. Jordan, P. Royl, G.A. Necker, R. Redlinger, A. Svishchev, "GASFLOW-III: A Computational Fluid Dynamics Code for Gases, Aerosols and Combustion, Volume 1: Theory and Computational Model," Karlsruhe Institute of Technology Report, Revision 3.5 (2014).
2. J. Xiao, J.R. Travis, T. Jordan, P. Royl, G.A. Necker, R. Redlinger, A. Svishchev, "GASFLOW-III: A Computational Fluid Dynamics Code for Gases, Aerosols and Combustion, Volume 2: User's Manual," Karlsruhe Institute of Technology Report, Revision 3.5 (2014).
3. H. Dimmelmeier, J. Eyink, M.A. Movahed, "Computational validation of the EPR combustible gas control system". Nuclear Engineering and Design 249, 118-124 (2012).
4. J. Xiao, et al., "Numerical analysis of hydrogen risk mitigation measures for support of ITER licensing," Fusion Engineering and Design 85, 205–214 (2010).
5. P. Royl, et al., "Analysis of steam and hydrogen distributions with PAR mitigation in NPP containments," Nuclear Engineering and Design 202, 231–248 (2000).
6. P. Kostka, et al., "Hydrogen mixing analyses for a VVER containment," In: 10th International Conference on Nuclear Engineering, Arlington, Virginia, USA (2002) (CD-ROM).

7. J. Kim, et al., "Spray effect on the behaviour of hydrogen during severe accidents by a loss of coolant accidents in the APR1400 containment," International Communications on Heat and Mass transfer 33, 1207–1216 (2006).
8. J. Xiao, J.R. Travis, et al., "Three-dimensional all-speed CFD code for safety analysis of nuclear reactor containment: Status of GASFLOW parallelization, model development, validation and application," Nuclear Engineering and Design 301 290–310 (2016).
9. P. Royl, J. Xiao, T. Jordan, "Blind Simulations of THAI Test TH27 with GASFLOW-MPI for Participation in the International Benchmark Conducted within the German THAI Program", Workshop Application of CFD/CFMD Codes (CFD4NRS_6) September 13-15, Cambridge, Ma, USA (2016).
10. "ANSYS FLUENT Theory Guide," Release 14.0 (2011).
11. G. Grotzbach, M. Worner, "Direct numerical and large eddy simulations in nuclear applications," International Journal of Heat and Fluid Flow, 20, 222-240 (1999).
12. Satish Balay, et al., "PETSc Users Manual", ANL-95/11 - Revision 3.5, Argonne National Laboratory (2014).
13. D. Gaston, C. Newman, G. Hansen, D. Lebrun-Grandié, "MOOSE: A parallel computational framework for coupled systems of nonlinear equations," Nuclear Engineering and Design 239, 1768–1778 (2009).
14. B.S. Kirk, J.W. Peterson, R.H. Stogner, and G.F. Carey, "libMesh: A C++ Library for Parallel Adaptive Mesh Refinement/Coarsening Simulations," Engineering with Computers, 22(3-4):237-254, (2006).
15. S.C. Crow, F.H. Champagne, "Orderly Structure in Jet Turbulence," J. Fluid Mech., 48, 547–591 (1971).
16. K.B. Zaman, A.K. Hussain, "Vortex Pairing in a Circular Jet under Controlled Excitation. Part 1. General Jet Response," J. Fluid Mech., 101, 449–544 (1980).
17. H.J. Hussein, S.P. Capp, and W.K. George, "Velocity Measurements in a High-Reynolds-Number, Momentum-Conserving, Axisymmetric, Turbulent Jet," J. Fluid Mech., 258, 31–75 (1994).
18. Jovic, s. and Driver, D.M., "Backward-facing step measurements at low Reynolds number, Re=5000," NASA Technical Memorandum NO: 108807, pp.1–24 (1994).
19. P.R. Spalart, "Direct simulation of a turbulent boundary layer up to Re=1410," Journal of Fluid Mechanics Digital Archive, 187, 61–98 (1988).
20. H. Le, P. Moin, and J. Kim, "Direct numerical simulation of turbulent flow over a backward-facing step," Journal of Fluid Mechanics, 330, 349–374 (1997).
21. B. Zhang, "Research and application of filtering grid scale and meshing adaptive-contronl strategy for large eddy simulation", Shanghai Jiao Tong University, Ph.D (2011).
22. B. Zhang, T. Wang, C. Gu and Y. Dai, "An adaptive control strategy for proper m e s h distribution in large eddy simulation, Journal of Hydrodynamics, 22(6):865-871, (2010).
23. R.V. Westphal and J.P. Johnston, "Effect of initial conditions on turbulent reattachment downstream of a backward-facing step," AIAA Journal, 22, 1727–1732 (1984).
24. Y. Dubief, F. Delcayre, "On coherent-vortex identification in turbulence," Journal of Turbulence, 1, 1–22 (2000).
25. J.L. Aider, A. Danet, "Large-eddy simulation study of upstream boundary conditions influence upon a backward-facing step flow," Comptes Rendus Mecanique, 334(7), 447–453 (2006).
26. B. Panjwani, I.S. Ertesvag, A. Gruber and K.E. Rian, "Large Eddy Simulation of Backward Facing Step Flow," 5th National Conference on Computational Mechanics, MekIT09, Trondheim, Norway (2009).